Application of the chiral forces to elctroweak processes

Vitalii Urbanevych

Ph.D. thesis written under the supervision of dr. hab Roman Skibiński
at the Jagiellonian University, Faculty of Physics, Astronomy
and Applied Computer Science, Kraków,
Sunday 3rd October, 2021

CONTENTS

1 Plan **2**

2 Formalism & numerical methods **5**
2.1 Deuteron bound state 5
2.2 2N scattering state 7
2.2.1 The Lippman-Schwinger equation 7
2.3 3N bound state 8
2.4 Nd scattering state 9
2.5 3N scattering state 10
2.6 Nuclear electromagnetic current 10
2.7 Theoretical uncertainties 10

3 Pion absorption at the lowest atomic orbital in ^{2}H, ^{3}H and ^{3}He **13**

4 Results **14**
4.1 Deuteron photodisintegraion 14
4.1.1 Cross section 14
4.1.2 Polarisation observables 16
4.2 Helium photodisintegration 17
4.2.1 3N photodisintegration 17
4.2.2 Nd photodisintegration 17

CHAPTER 1

PLAN

- Why we study few nucleon systems
  - Strong interactions (2N and 3N force investigation; QCD, relativistic effects)
  - Electro-magnetic processes (electrons-, photons-induced reactions) (Arenhovel did ...)
  - Weak interactions (neutrons)
- Nuclear forces used in the thesis
  - AV18
  - Chiral (scs, sms; difference between chiral models; regularization problem)
- Currents used in the thesis (regularization of currents to be done)
- Formalism & numerical methods
  - Lippman-Schwinger eq
  - Schrodinger eq for deuteron; wave functions (sms) for deuteron - figures, binding energy
  - Three body: Fadeev eq. for bound (He3, H3) and scattering states
  - Siegert theorem ?
  - Partial wave decomposition, states ($pq\alpha$), Jakobi momenta; operators in PW decomp. (current); Mathematica for PW
  - Theoretical uncertainties: truncation error, cut-off dependency, chiral order dependency
- Results (**find everything what I have calculated: all processes and energies**)
  - H2 photodisintegration
  - He3 and H3 photodisintegration
  - Pion capture

- Summary
- References

Why we study few nucleon systems

The study of light nuclei for the decades has been serving as an easiest way to study NN systems and forces inside the atom. And convenient way to proceed may be an interaction of atom with other particles: elastic or inelastic scattering. It is possible to construct such an experiments and check if theory works. People take into account that interactions may be caused by different forces and therefore should be described in different ways. It can be either strong, weak or electromagnetic interaction. It depends on the type of particle being scattered and the target which reaction it is.

In order to proper describe the nuclear reactions many factors should be taken into account. First of all, different nuclear forces may act on the participants.

The strong nuclear force appear inside the nuclei and among others bound neutrons and protons together. The description of strong interactions is extremely difficult as it deals not only with nucleon, but with their constituents: quarks and gluons. Quantum Chromodynamics(QCD) is a modern theory describing strong interactions, but it has also its limitations at the moment as it is not reliable at low energies ($Q^2 \lesssim 1GeV^2$). So other approaches are coming into the scene such as chiral effective theory, lattice calculation and others [**?**].

Electromagnetic force appears between charged particles like protons and electrons. Also, the force is transferred between charged particles with a photon, so in photon- and electron- scatterings on the nuclei an electromagnetic force is playing an important role. Arenhovel [**?**] studied electromagnetic process - Deuteron photodisintegration, applying different approaches and comparing the results with experimental data.

The weak force...

...

Starting the study of 3- (and more) nucleon systems it was found that 2N force is not enough to describe the system and 3N force was introduced. The first applications of such a force showed that it brings sufficient contribution and cannot be ignored [**?**]. Whereas the first applications included only early "realistic" potential, the latter investigations only proved this statements [**?**, **?**]. It was also used to construct four-nucleon (4N) bound state [**?**].

...

Nuclear forces used in the thesis

In order to construct a potential people often use phenomenological or semi-phenomenological approaches. It allows to combine theoretical knowledge about processes and experimental data.

One of such potentials, which was used in current thesis is Argonne V18 (AV18) [**?**] In order to construct NN force, authors combine analytical electromagnetic and one-pion-exchange parts with phenomenological one, fitting parameters to the Nijmegen partial-wave analysis of *pp* and *np* data [**?**]. Authors showed, that AV18 potential delivers good results in the description of nucleon scattering data as well as deuteron properties.

In the early 1990-ies Weinberg [**?**, **?**] introduced an idea of using a most general Lagrangian satisfying assumed symmetry principles and in particular spontaneously broken

chiral symmetry to describe nuclear interactions at low energies. This idea together with effective field theory (EFT) of Quantum chromodynamics (QCD) led to the development of Chiral effective field theory (χEFT) which nowadays has become one of the most advanced approach to describing nuclear reactions at low energies.

For the EFT it is very important to define a quantity, which powers will determine a perturbation order. In the χEFT there are two natural scales: so-called soft scale - the mass of Pion $Q \sim M_\pi$ and hard scale - $\Lambda_\chi \sim 1\ GeV$ (chiral symmetry breaking scale). The ratio between these two scales $(Q/\Lambda_\chi)^\nu$ is being used as an expansion parameter in χEFT with power ν.

Considering so-called irreducible (the diagrams that cannot be split by cutting nucleon lines), Weinberg [**?**, **?**] came to the identity for the powers of such diagrams [**?**]:

$$\nu_W = 4 - A - 2C + 2L + \sum_i \Delta_i, \tag{1.1}$$

where

$$\Delta_i \equiv d_i + \frac{n_i}{2} - 2 \tag{1.2}$$

In 1.1, C is a number of pieces which are connected, L - the number of loops in the graph. In 1.2, n_i is a number of nucleon field operators, d_i - the number of insertions (or derivatives) of M_π.

In χEFT the first order is called "leading order" (LO) and it is followed by next-to-leading order (NLO), next-to-next-to-leading order (N2LO) and so on. At the moment, the highest order for which there is a derived term in potential is N4LO. Also some contributions from N5LO are included in the N4LO+ chiral order.

As pointed above, for many-nucleon systems it is important to include not only nucleon-nucleon interaction to the potential, but also a 3- and many- nucleon contributions. In the χEFT 3N force contributes starting from N2LO and 4N force is presented starting from N3LO, so there is a systematic way to include all the forces from simplest diagrams at LO and gradually adding more and more terms. It is also beneficial in the way that one can obtain results using chiral potential at different orders and track which one gives larger or smaller contribution (changes in the final results).

The χEFT may be applied both in coordinate and momentum spaces. Nevertheless in both cases it requires regularization which is cutting low coordinate values in order to avoid infinities (or high momentum values - in momentum space). The value at which the cut is applied (cut-off value) is not fixed and usually calculations are being performed for different cut-off values. The comparison of such results may reveal stronger or weaker dependance and in perfect case one will come up with such a potential, were the cut will not affect results much.

The potential may be transformed from coordinate to momentum space (or vice versa), but it is important at which frame the regularization was performed and what was a regularization function. That's why there are different versions of chiral potential. One is semi-local coordinate space regularized potential (SCS) [**?**] and another one is similar, but with regularization applied in momentum space (SMS potential) [**?**].

Currents

CHAPTER 2

FORMALISM & NUMERICAL METHODS

In order to calculate any observable for the Deuteron photodisintegration, one has to find a nuclear matrix elements:

$$N^{\mu} = \langle \Psi_f \vec{P}_f \mid \frac{1}{e} J^{\mu}(0) \mid \Psi_i \vec{P}_i \rangle = \langle p'(l's')j'm'_j t' m'_t \vec{P}_f \mid J^{\mu} \mid \phi_d m_d \vec{P}_i \rangle, \tag{2.1}$$

where J^{μ} is a four-vector current operator which acts between initial and final two-nucleon states.

2.1 Deuteron bound state

Let's find a deuteron bound state wave function ϕ_d. The time-independent Schrodinger equation for two particles in such case will be:

$$(H_0 + V) \mid \psi_{12} \rangle = E_d \mid \psi_{12} \rangle, \tag{2.2}$$

with a kinetic energy H_0 and potential V. The kinetic energy H_0 can be represented in terms of relative and total momenta of the particles:

$$H_0 = \frac{\vec{p}_1^{\,2}}{2m_1} + \frac{\vec{p}_2^{\,2}}{2m_2} = \frac{\vec{p}^{\,2}}{2\mu} + \frac{\vec{\mathcal{P}}^2}{2M}, \tag{2.3}$$

where relative and total momenta are defined as follows:

$$\vec{p} = \frac{(m_1\vec{p}_1 - m_2\vec{p}_2)}{m_1 + m_2} \tag{2.4}$$

$$\vec{\mathcal{P}} = \vec{p}_1 + \vec{p}_2 \tag{2.5}$$

and $M = m_1 + m_2$ is a total mass, $\mu = \frac{m_1 m_2}{M}$ is a relative mass of two nucleons.

We are working in the momentum space, so acting by the momentum operator on the Eq.(2.2) one can obtain two separated equations:

$$\frac{\vec{p}^2}{2\mu}\langle\vec{p}\mid\Psi_{int}\rangle+\int d\vec{p}'\langle\vec{p}\mid V\mid\vec{p}'\rangle\langle\vec{p}'\mid\Psi_{int}\rangle=(E_d-E_{c.m.})\langle\vec{p}\mid\Psi_{int}\rangle \tag{2.6}$$

$$\frac{\vec{\mathcal{P}}^2}{2M}\langle\mathcal{P}\mid\Psi_{c.m.}\rangle=E_{c.m.}\langle\mathcal{P}\mid\Psi_{c.m.}\rangle \tag{2.7}$$

Eq.(2.6) is basically a Schrodinger equation for one particle with mass μ and Eq.(2.7) can be regarded as a Schrodinger equation for particle with mass M in a free motion. Assuming that deuteron is at rest ($E_{c.m.}=0$) we can stick to the Eq.(2.6) only. So that:

$$\frac{\vec{p}^2}{2\mu}\langle\vec{p}\mid\Psi_{int}\rangle+\int d\vec{p}'\langle\vec{p}\mid V\mid\vec{p}'\rangle\langle\vec{p}'\mid\Psi_{int}\rangle=E_d\langle\vec{p}\mid\Psi_{int}\rangle \tag{2.8}$$

Next we move to the partial-wave representation of the momentum state in the following form:

$$\mid\vec{p}\rangle=\mid p\alpha\rangle\equiv\mid p(ls)jm_j\rangle\mid tm_t\rangle, \tag{2.9}$$

where we introduce quantum numbers l, s ,j ,t as orbital angular momentum, total spin, total angular momentum and total isospin respectively. m_j and m_t are isospin and spin projections.

Yet one can introduce simpler states than it is in (2.9).

$$\mid p(ls)jm_j\rangle=\sum_{m_l}c(lsj;m_l,m_j-m_l,m_j)\mid plm_l\rangle\mid s\ m_j-m_l\rangle \tag{2.10}$$

Also we can decompose spin and isospin states as follows:

$$\mid sm_s\rangle=\sum_{m_1}c(\frac{1}{2}\frac{1}{2}s;m_1,m_s-m_1,m_s)\mid\frac{1}{2}m_1\rangle\mid\frac{1}{2}m_s-m_1\rangle \tag{2.11}$$

$$\mid tm_t\rangle=\sum_{\nu_1}c(\frac{1}{2}\frac{1}{2}t;\nu_1,m_t-\nu_1,m_t)\mid\frac{1}{2}\nu_1\rangle\mid\frac{1}{2}m_t-\nu_1\rangle \tag{2.12}$$

In Eqs.(2.10) -(2.12), $c(...)$ are Clebsh-Gordon coefficients. Nucleons are spin $\frac{1}{2}$ particles, and also we treat proton and neutron as the same particle in different isospin states, so that isospin is $\nu_1=\frac{1}{2}$ for proton and $\nu_1=-\frac{1}{2}$ for neutron.

The states $\mid plm_l\rangle$ from Eq.(2.10) are orthogonal, so that

$$\langle p'l'm_l'\mid plm_l\rangle=\frac{\delta(p-p')}{p^2}\delta_{ll'}\delta_{m_lm_l'} \tag{2.13}$$

and also satisfy the completeness relation:

$$\sum_{l=0}^{\infty}\sum_{m_l=-l}^{l}\int dpp^2\mid plm_l\rangle\langle plm_l\mid=\mathbb{1} \tag{2.14}$$

These states also fulfill a relation

$$\langle\vec{p}'\mid plm_l\rangle=\frac{\delta(|\vec{p}'|-p)}{p^2}Y_{lm_l}(\hat{p}'), \tag{2.15}$$

where $Y_{lm_l}(\hat{p}')$ is a spherical harmonic and 'hat' means a unit vector.

If we exchange nucleons 1 and 2 there should be a sign change and this requirement

can in mathematical form can be expressed as:

$$(-1)^{l+s+t} = -1 \tag{2.16}$$

Taking into account Eq.(2.16), one can find only one possible case for the deuteron bound state: 2 coupled channels for l=0,2; s=1; j=1and $t = m_t = 0$. These 2 channels are usually denoted as ${}^3S_1$ and ${}^3D_1$ and corresponding wave functions are $\phi_0(p)$ and $\phi_2(p)$.

So with a new basis Eq.(2.8) takes a form:

$$\frac{\vec{p}^2}{2\mu}\phi_l(p) + \sum_{l'=0,2}\int dp' p'^2 \langle p l m_l \mid V \mid p' l' m_l' \rangle \phi_{l'}(p) = E_d \phi_l(p), \tag{2.17}$$

for $l = 0, 2$. Assuming that one has a matrix elements for the potential $\langle p l m_l \mid V \mid p' l' m_l' \rangle$, there is still one complication in the Eq.(2.17) - integration. In order to get rid of the integral I use a Gaussian quadrature method of numerical integration [**?**]. It allows to replace an integral by the weighted sum: $\int_a^b f(x)dx = \sum_{i=1}^n \omega_i f(x_i)$ In current work I used 72 points in the interval from 0 to $50fm$. Using this method, Eq.(2.8) becomes

$$\frac{\vec{p}^2}{2\mu}\phi_l(p) + \sum_{l'=0,2}\sum_{j=0}^{N} \omega_j p_j'^2 \langle p_j l m_l \mid V \mid p_j' l' m_l' \rangle \phi_{l'}(p) = E_d \phi_l(p), \tag{2.18}$$

It is possible to solve this equation as an eigenvalue problem $M\Psi = E_n\Psi$ and find simultaneously wave function values and binding energy E_n.

2.2 2N scattering state

2.2.1 The Lippman-Schwinger equation

Let us start from the time-independent formulation of the scattering process. In such a case Hamiltonian will be:

$$H = H_0 + V, \tag{2.19}$$

where H_0 is a kinetic energy operator $H_0 = \frac{\vec{p}^2}{2m}$. For a free particle motion, V will be absent and we will denote an energy eigenstate as $\mid \vec{p} \rangle$ - a free particle state. In the case of the scattering process, the eigenstate will differ from $\mid \phi \rangle$, but in case of elastic scattering (which we re interested in) the energy eigenvalue E should be the same.

So below I write a system of Schrodinger equations for such scattering process:

$$\begin{cases} H_0 \mid \vec{p} \rangle & = E \mid \vec{p} \rangle \\ (H_0 + V) \mid \psi \rangle & = E \mid \psi \rangle \end{cases} \tag{2.20}$$

I would like to find such a solution to Eq. (2.20), so that $\mid \psi \rangle \rightarrow \mid \vec{p} \rangle$ with $V \rightarrow 0$ and both $\mid \psi \rangle$ and $\mid \vec{p} \rangle$ have the same energy eigenvalues E. As we have scattering process, the energy spectra for both operators H_0 and$H_0 + V$ are continuous.

From Eq. (2.20) follows that

$$\mid \psi \rangle = \frac{1}{E - H_0} V \mid \psi \rangle + \mid \vec{p} \rangle, \tag{2.21}$$

where $\mid \vec{p}\rangle$ was added artificially in order to satisfy a criterion mentioned above and following the logic from [**?**]. In addition, it guarantees that application of the operator $(E - H_0)$ to the (2.21) results in the second equation from the system (2.20).

In order to deal with a singular operator $\frac{1}{E-H_0}$ in eq.(2.21), the well-known technique is to make such an operator slightly complex by adding small imaginary number to the denominator so Eq.(2.21) becomes

$$|\psi\rangle = G_0(E \pm i\epsilon)V \mid \psi\rangle + \mid \vec{p}\rangle, \tag{2.22}$$

where G_0 is a free propagator:

$$G_0(z) = \frac{1}{z - H_0} \tag{2.23}$$

Solution with $G_0(E-i\epsilon)$ corresponds to the incoming spherical wave, while $G_0(E-i\epsilon)$ - to the outgoing one. Since we are interested in the scattering process, we will use the $(+)$ sign further.

Eq. (2.22) is known as a Lippman-Schwinger equation (LSE) and using the definition of the transition operator t:

$$t\,|\vec{p}\rangle = V\,|\psi\rangle \tag{2.24}$$

we can rewrite it as

$$|\psi\rangle = (1 + G_0(E + i\epsilon)Vt)\,|\vec{p}\rangle \tag{2.25}$$

With substitution of Eq. (2.22) into Eq. (2.24) we can find an explicit form of the t operator:

$$\begin{aligned} t\,|\vec{p}\rangle &= VG_0(E + i\epsilon)V \mid \psi\rangle + V \mid \vec{p}\rangle = \\ &= VG_0(E + i\epsilon)t\,|\vec{p}\rangle + V \mid \vec{p}\rangle \end{aligned} \tag{2.26}$$

Getting rid of the initial state $|\vec{p}\rangle$ in the Eq. (2.26) we can get a LSE for the transition operator in the iterative form:

$$\begin{aligned} t &= V + VG_0Vt = \\ &= V + VG_0V + VG_0VG_0V + ... \end{aligned} \tag{2.27}$$

Using Eq. (2.25) we can write Eq. (2.1) as

$$N^\mu = \langle \phi m_p m_n |\,(1 + G_0(E + i\epsilon)Vt)\frac{1}{e}J^\mu(0) \mid \Psi_i \vec{P}_i\rangle \tag{2.28}$$

2.3 3N bound state

The 3N bound state is derived from a general Schrodinger for 3N system and its total wave function obeys the following equation:

$$|\Psi_i\rangle = G_0(E+i\epsilon)\sum_{j=1}^{3}(V_j+V_4^j)\,|\Psi_i\rangle\,, \tag{2.29}$$

where G_0 is a free propagator from Eq. (2.23), V_j - is a two-body potential acting between nucleons k and l (j, k and l - are the numbers of each nucleon) and V_4^j is a component of three-body potential $V_4 = \sum_{j=1}^{3} V_4^j$. E - is a binding energy.

Eq. (2.29) can be split into 3 independent equations for so-called Faddeev components $|\psi_j\rangle$

$$|\Psi_i\rangle = \sum_{j=1}^{3}|\psi_j\rangle\,. \tag{2.30}$$

Using Eq. (2.30) one can decompose Eq. (2.29) into separate equations for each Faddeev component:

$$|\psi_j\rangle = G_0(E+i\epsilon)(V_j+V_4^j)\,|\Psi_i\rangle\,, \tag{2.31}$$

Next I introduce a permutation operator P, which is a combination of operators P_{jk}:

$$P = P_{12}P_{23} + P_{13}P_{32}. \tag{2.32}$$

The operator component P_{jk} acting on the state interchange the momenta and quantum numbers of the nucleon number j and$k$.

Using Eq. (2.32) and Eq. (2.30), one can rewrite Eq. (2.31) in the following form:

$$|\psi_j\rangle = G_0(E+i\epsilon)t_jP\,|\psi_i\rangle + (1+G_0(E+i\epsilon)t_j)G_0(E+i\epsilon)V_4^j(1+P)\,|\psi_i\rangle\,, \tag{2.33}$$

where t_j is a two-body t-operator which obeys Eq. (2.26) for corresponding two-body potential V_j.

2.4 Nd scattering state

Analogously to the bound state, one can express a nucleon-deuteron scattering state using a permutation operator Eq. (2.32).

$$\left|\Psi^{(-)}\right\rangle^{Nd} = \frac{1}{\sqrt{3}}(1+P)\left|\Psi_1^{(-)}\right\rangle^{Nd} \tag{2.34}$$

A scattering state $\left|\Psi_1^{(-)}\right\rangle^{Nd}$ can be expressed in terms of asymptotic state $\left|\Phi_1^{Nd}\right\rangle$, where particles 2 and 3 form a deuteron and the third particle (number 1) is a nucleon which propagates freely with relativemomentum $\vec{q}_0$ with respect to the deuteron:

$$\left|\Psi_1^{(-)}\right\rangle^{Nd} \equiv \lim_{\epsilon\to 0} i\epsilon G(E_{Nd}-i\epsilon)\left|\Phi_1^{Nd}\right\rangle \tag{2.35}$$

$$\left|\Phi_1^{Nd}\right\rangle \equiv \left|\Phi_{d(2,3)}\right\rangle|\vec{q}_0\rangle\,, \tag{2.36}$$

where $\left|\Phi_{d(2,3)}\right\rangle$ is a deuteron wave function and $|\vec{q}_0\rangle$ - a free particle state. E_{Nd} is a total

energy of the 3N system:

$$E_{Nd} = E_d + \frac{3|\vec{q}_0|^2}{4m}, \tag{2.37}$$

where E_d is a deuteron binding energy and m - nucleon mass.

The full propagator $G(E_{Nd})$ in this case takes a form:

$$G(z) = \frac{1}{z - (H_0 + \sum_{i=1}^{4} V_i)} \tag{2.38}$$

2.5 3N scattering state

As in Sec. 2.4, one can write an equation for the 3-nucleone scattering state:

$$\left|\Psi^{(-)}\right\rangle^{3N} = \frac{1}{\sqrt{3}} \left|\Psi_j^{(-)}\right\rangle^{3N} \tag{2.39}$$

with a set of corresponding equations for $\left|\Psi_j^{(-)}\right\rangle^{3N}$

$$\left|\Psi_j^{(-)}\right\rangle^{3N} \equiv \lim_{\epsilon\to 0} i\epsilon G(E_{3N} - i\epsilon) \left|\Phi_j^{3N}\right\rangle \tag{2.40}$$

$$\left|\Phi_j^{3N}\right\rangle \equiv \frac{1}{\sqrt{2}}(1 - P_{kl}) \left|\vec{p}(kl)\vec{q}(j)\right\rangle \tag{2.41}$$

$$E_{3N} = \frac{|\vec{p}|^2}{m} + \frac{3|\vec{q}|^2}{4m}, \tag{2.42}$$

2.6 Nuclear electromagnetic current

2.7 Theoretical uncertainties

Truncation error

As it was mention above, each subsequent order of chiral expansion provide us with more and more sophisticated potential. Starling from the leading order (LO) and coming to next N2LO, N3LO and so on we toke into account more Feynmann diagrams and in result potential is able to provide us with more precise predictions for the regarded process and observable. But the chiral expansion (as any expansion) in principle can be continued to the infinity, improving the resulting series. In practice we are limited by some number of terms, but we would like to find out the uncertainty appearing from cutting off remaining part of the expansion. This uncertainty is called a truncation error and there some ways of estimation its value for the potential of each order of chiral expansion having predictions for some limited number of terms [?, ?, ?, ?].

Let's regard some observable $X^i(p)$ which is calculated at i-s order of chiral expansion with expansion parameter Q ($i = 0, 2, 3...$)[1]. Here p specifies ????? a momentum scale of the current reaction in the center of mass frame (in the case of deuteron photodisintegration it would be a photon's momentum).

[1] We do not have a first order of expansion because this term in chiral expansion is always vanished and NLO corresponds to the quadratic term (number 2)

If I define a difference between observable at each subsequent orders as:

$$\Delta X^{(2)} = |X^{(2)} - X^{(0)}|, \Delta X^{(i>2)} = |X^{(i)} - X^{(i-1)}|, \tag{2.43}$$

then chiral expansion for X can be written as:

$$X = X^{(0)} + \Delta X^{(2)} + \Delta X^{(3)} + ... + \Delta X^{(i)} \tag{2.44}$$

The truncation error at order i $\delta X^{(i)}$ is estimated using actual and expected values of the observable at higher orders. In order to do that I use following expressions:

$$\delta X^{(0)} = Q^2 \left|X^{(0)}\right| \tag{2.45}$$

$$\delta X^{(i)} = \max_{2\leq j\leq i} \left(Q^{i+1} \left|X^{(0)}\right|, Q^{i+1-j} \left|\Delta X^{(j)}\right|\right) \tag{2.46}$$

Additionally, following the [?] I use the actual high-order predictions in order to specify uncertainties so that:

$$\delta X^{(i)} \geq \max_{j,k}(|X^{j\geq i} - X^{k\geq i}|) \tag{2.47}$$

and to be conservative I use additional restriction:

$$\delta X^{(i)} \geq Q\delta X^{(i-1)} \tag{2.48}$$

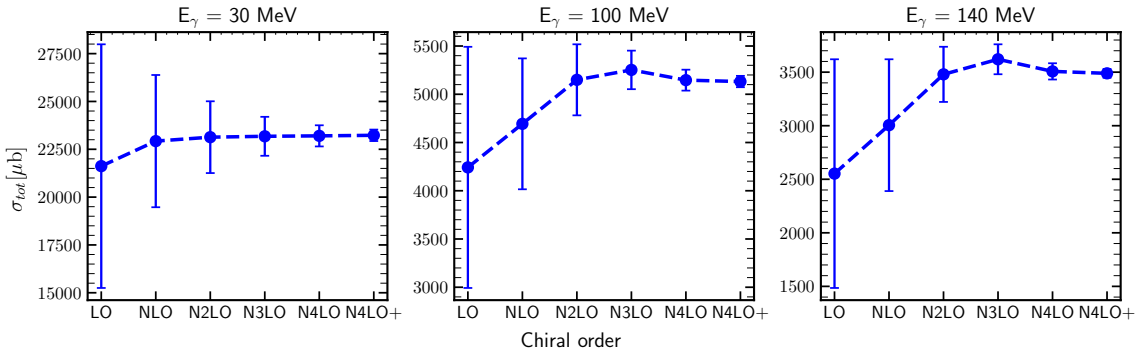

Figure 2.1: Total cross section of the deuteron photonisintegration process as a dependance on the chiral order for three photon energy E_γ values: 30, 100 and 140 MeV. Error bands show an estimated truncation error at each order.

In Fig. 2.1 I present a total cross-section for the deuteron photodisintegration at 3 photon energie values: 30,100 and140 MeV as a dependance on the chiral order. Error bands show truncation errors calculated using described above method. One can see that errors are being reduced with each consecutive chiral order: for LO it is the biggest while for N4LO+ it is hardly visible at presented scale.

Cutoff dependency

Another uncertainty comes from the choice of the cutoff parameter's value. The SMS potential is being regularized using the Gaussian form factor $F(\vec{l}^2)$:

$$F(\vec{l}^2) = e^{-\frac{\vec{l}^2+M_\pi^2}{\Lambda^2}}, \tag{2.49}$$

where M_π is an effective pion mass and Λ - is a cutoff parameter.

The form factor from Eq. (2.49), being used together with Feynman propagator, ensures that long-range part of the forces has no singularities.

According to [**?**], where the SMS potential was presented, 4 values of the cutoff parameter Λ are recommended: 400, 450, 500 and 550 MeV. Using each of them one obtains different predictions which may differ from actual (experimental) value. Therefore the choice of Λ value may affect a quality of the prediction.

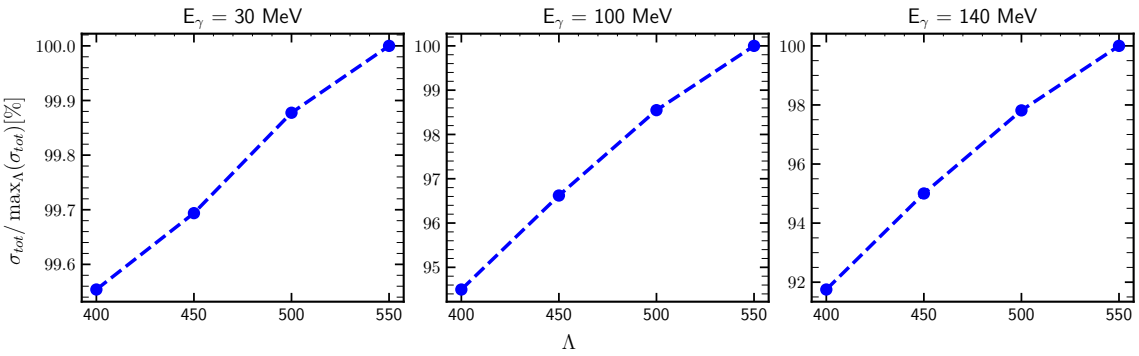

Figure 2.2: Total cross section of the deuteron photonisintegration process as a dependance on the cutoff parameter Λ for three photon energy E$_\gamma$ values: 30, 100 and 140 MeV.

The comparison of predictions obtained with different values of the cutoff parameter Λ is presented on the Fig. 2.2. Each subfigure shows a predictions for the total cross section as a function of the cutoff parameter for the photons energies 30, 100 and 140 MeV normalized be the maximum value among all Λ (at the chiral order N^{4}LO+). As we can see, there is almost linear dependance with positive linearity coefficient value: with higher Λ the cross section value increases as well. The noticeable is also the fact, that with higher photon's energy, the cutoff dependance becomes stronger: fro $E_\gamma = 30$ MeV the maximal difference between predictions is around 0.5% while for 140 MeV it increases to more than 8%. This results are generally within our beliefs that our model works better for smaller energies.

CHAPTER 3

PION ABSORPTION AT THE LOWEST ATOMIC ORBITAL IN ^{2}H, ^{3}H AND ^{3}HE

CHAPTER 4

RESULTS

4.1 Deuteron photodisintegraion

4.1.1 Cross section

In this section I will show the results of my calculation starting from the deuteron photodisintegration process. One of the most studying observable is obviously cross section. There is a number of papers which present measurement results for both differential and total cross section [?, ?, ?, ?, ?, ?, ?, ?, ?, ?] so it is convenient to prepare a theoretical predictions in order to compare it with experimental results.

On the Fig. 4.1 and Fig. 4.2 I present predictions for the total cross section σ_{tot} [μb] which I obtained using the chiral potential at the order N^{4}LO+ and with the cutoff parameter $\Lambda = 450$ MeV (my best predictions). Looking at Fig. 4.1, we can see that at low photon energies (below 50 MeV) my predictions which include 2N contributions using Siegert approach, describe experimental results quite well. We can suppose that the difference with experimental data may come from the statistical uncertainty of the data itself, as my predictions are often in between the data from different sources. Moreover even at such low energies the 1N current is clearly not enough to describe this observable as dashed pink line has much lower values and the difference becomes even larger with larger photon's energies.

Having look at the higher energies (above 50 MeV, Fig. 4.2) we can notice that the difference with experimental data is not only quantitative, but also qualitative. There is a peak around 300 MeV in the experimental data from [?] which is not reflected in my predictions. The reason of such discrepancy is most likely coming from the relativistic effects which I do not take into account. At higher energies their contribution becomes larger and here we observe a clear justification of such a lack. It is also confirmed by the calculations in [?] where authors present predictions obtained with and without including relativistic effects and such a peak appears in the latter case.

Nevertheless my main goal is to describe deuteron photodisintegration at low energies and predictions seem to be well describing experimental data at $E_\gamma \lesssim 50$ MeV. The higher energies region is presented in order to investigate how far the predictions are from experimental results and what can be improved in the future (e.g. include relativistic part).

Maybe better reorganize figures, combine similar figures for different energies in one?

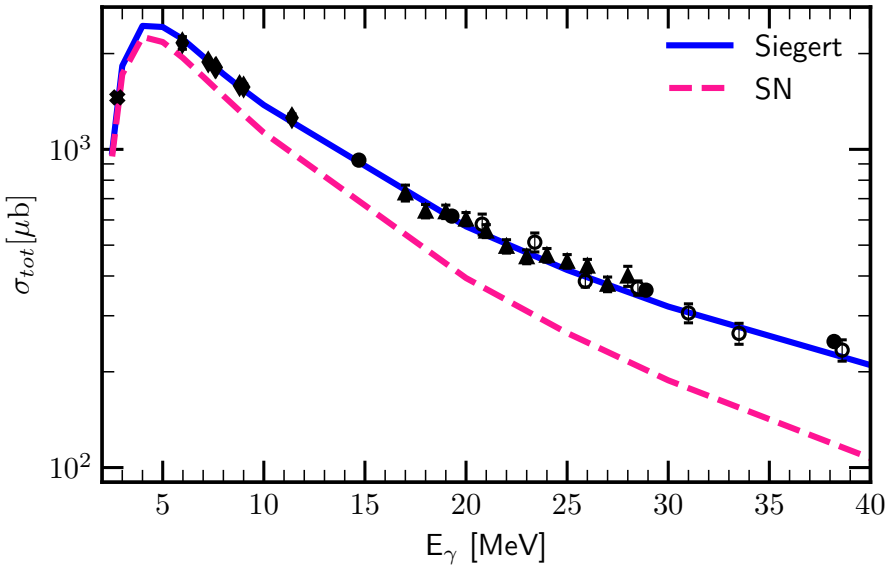

Figure 4.1: The same as on the Fig. 4.2 but for the energy range 2.5 - 40 MeV.

Figures 4.3 - 4.5 show my predictions for the differential cross section $\frac{d\sigma}{d\Omega}$, where each subfigure presents results obtained using different values of the photon energy: 30, 100 and 140 MeV. Fig. 4.3 shows the predictions obtained using different chiral orders (from LO to N^{4}LO+) and with $\Lambda = 450$ MeV. Comparing the best predictions (N^{4}LO+, $\Lambda = 450$ MeV) for each subfigure, we can once more conclude that the higher photon's energy is, the larger is difference between the theoretical predictions and experimental measurements. At $E_\gamma = 30$ MeV (top pane) my predictions almost perfectly match the data and the difference is almost always within the experimental uncertainties. Going to the energy 100 MeV (middle subfigure) the descriptions seems not to be such good: theoretical predictions match experimental data qualitatively, but the gap in the angles range ($60° < \theta_p < 130°$) is around 30% (check the value!). Looking at the bottom figure, it is even hard to say about good qualitative description: the general trend of the angular dependance is presented, but still the predictions are far from experimental values. In addition, figures for each energy confirm the convergence of the predictions with respect to the chiral order. We see that the curves at LO are far from both experimental data and the best potential's predictions (N^{4}LO+) and the higher is photon's energy, the larger is this difference. With each subsequent chiral order, the curves are more closer to each other and the difference between N^{4}LO and N^{4}LO+ is hardly visible at current scale. So I can conclude that predictions are converged and further chiral orders would rather not bring large contribution to the cross section values. What may be helpful for a better data description is a 2N current and relativistic correction, mentioned earlier.

The Fig. 4.4 presents theoretical (truncation) uncertainties and it once more confirms that for the regarded nuclear reaction chiral order N^{4}LO+ is able to produce converged predictions: the black band is hardly visible for the $E_\gamma = 30$ MeV and is also quite narrow for larger energies. The difference with experimental data is rather systematic and is independent on the chiral order.

Fig. 4.5 presents a cutoff dependency of my predictions. The ideal case is when the dependency is so weak that the choice of the parameter Λ would not make large changes. In practice the choice of this parameter can be important as it makes a noticeable

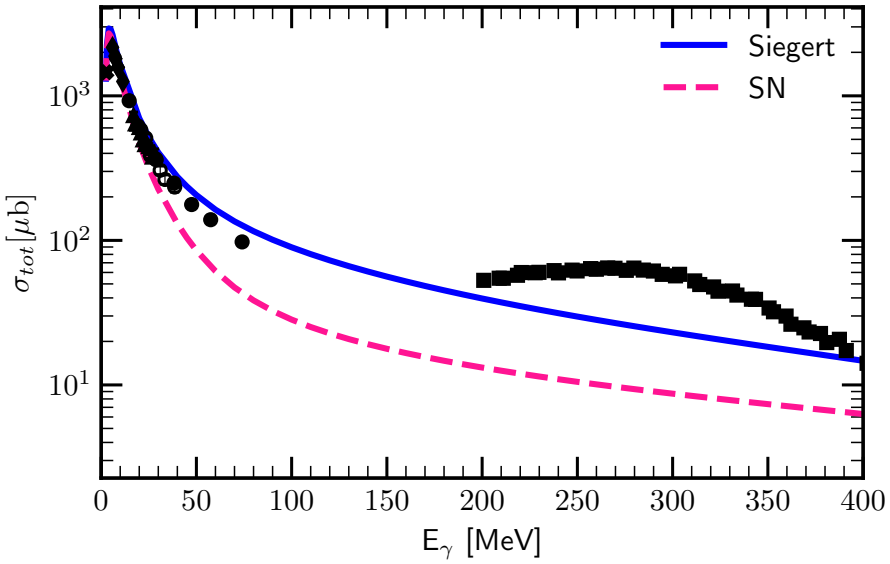

Figure 4.2: Total cross section as a function of the photon's energy E_γ. Solid blue line presents results obtained with SN+Siegert and dashed pink line - with only SN current. The experimental data are from [?] (black filled circles), [?] (empty circles), [?] (squares), [?] (triangles), [?] (cross "X") and [?] (dimonds).

difference in predictions.

On the top figure the cutoff dependance is so weak, that, in fact, all the lines (for different Λ values) overlap each other and we cannot distinguish them with the naked eye. Nevertheless, with increasing photon's energy to 100 and 140 MeV (middle and bottom figures) the spread becomes larger. Although the spread is visible, it is not so large and even for 140 MeV it is within 12%.

On the Fig. 2.2 we saw that the total cross section for the same energies has the cutoff spread around 4.5% for 100 MeV and 8% for 140 MeV. For 30 MeV it is below 1%.

4.1.2 Polarisation observables

maybe reorganize similar to cross section?

In this subsection I will present my predictions for selected polarisation observables. I start with deuteron analyzing power T_{20}, T_{21} and T_{22}, which according to [?] are defined as:

$$T_{2i}(\theta) = \frac{(2-\delta_{i0})\,\mathrm{Re}\,V_{2i}}{V_{00}}, i = 0, 1, 2 \tag{4.1}$$

On the Figures 4.6, 4.7 and 4.8 I show my predictions for the T_{20}, T_{21} and T_{22} respectively as a functions of the outgoing proton angle θ in the CM frame. Each of them is prepared with photon's energy 100 MeV and is organized in the similar way: the top pane shows a dependance of the predictions on the chiral order of the potentia. The middle subfigure is showing a correspondent truncation error for each of the predictions from a top one (without LO, because its uncertainty is too large and will make the readability worse). The last (bottom) pane shows the cutoff dependance for each observable at the chiral order N^4LO+. The energy 100 MeV was chosen as an intermediate value with respect to results presented in 4.1.1.

All the polarisation observables presented here, show a good convergence upon a chiral order as it is hard to distinguish the predictions from each subsequent order starting from the N^{2}LO. The figures for the truncation errors confirm this conclusion: we can see that only the band for NLO is recognizable, while other errors are almost overlapping each other with the current scale.

The cutoff dependency for T_{20} and T_{21} is weak and predictions for each value of the Λ are hardly separable with the naked eye. The T_{22} component, in the turn, has slightly stronger discrepancy as at the stationary point around 90° we can see the difference between each of the curves, which still is small.

On the next figures, I show the predictions in a similar way as it was done in [**?**] in order to compare my predictions with the experimental data. On the Figures 4.9 - 4.15 I show an angular dependance of the T_{2i} ($i = 0, 1, 2$) for a specific energy bands. Solid blue line shows an average value of the observable in the specified energy range obtained at N^{4}LO+ with $\Lambda = 450$ MeV, while the pink dashed line is a prediction obtained with a same setup but without using a contributions from Siegert approach (single nucleon current only). Bands for each of prediction specify the spread of predictions in regarded energy band.

One can see that the data description is better for the predictions with Siegert contributions and SN current is not able to describe experiment properly. With increasing energy (more than 100 MeV), the difference between predicted values and experimental data becomes larger (especially for T_{22}), but the model I use is not meant to be used for high energies and figures are presented out of the curiosity.

On the Figure 4.16 the energy dependance of T_{20} and T_{22} (integrated over all angles) is presented for the energy range 0-400 MeV. I also demonstrate the experimental data from [**?**] and [**?**] as well as theoretical calculations from [**?**] on the figure. For T_{20} the model is able to describe experimental data well even for high energies. On the other hand, T_{22} is not so well described: for the low energies the prediction curve is somehow within uncertainties of experimental data, but further the difference with the data becomes larger. Also it is not reflect the qualitative nature of the data as we can see that after around 150 MeV data points start ascending which is not represented in my predictions. Theoretical predictions from [**?**] (brown dashed curve) are also not able to describe data quantitatively for T_{22}, but the growth is presented there.

Similar situation is on the Figures 4.17 and 4.18 where I show an energy dependance of Deuteron analyzing power components for specific angular ranges (following the data from [**?**]). Predictions for T_{20} are able to reflect the experimental results, while for T_{21} and T_{22} predictions are reasonable (quantitative-wise) only for lower energies and difference with data becomes larger when energy increases. Predictions for T_{22} once more confirm an insufficiency of SN and an importance of 2-nucleon current contributions.

4.2 Helium photodisintegration

4.2.1 3N photodisintegration

4.2.2 Nd photodisintegration

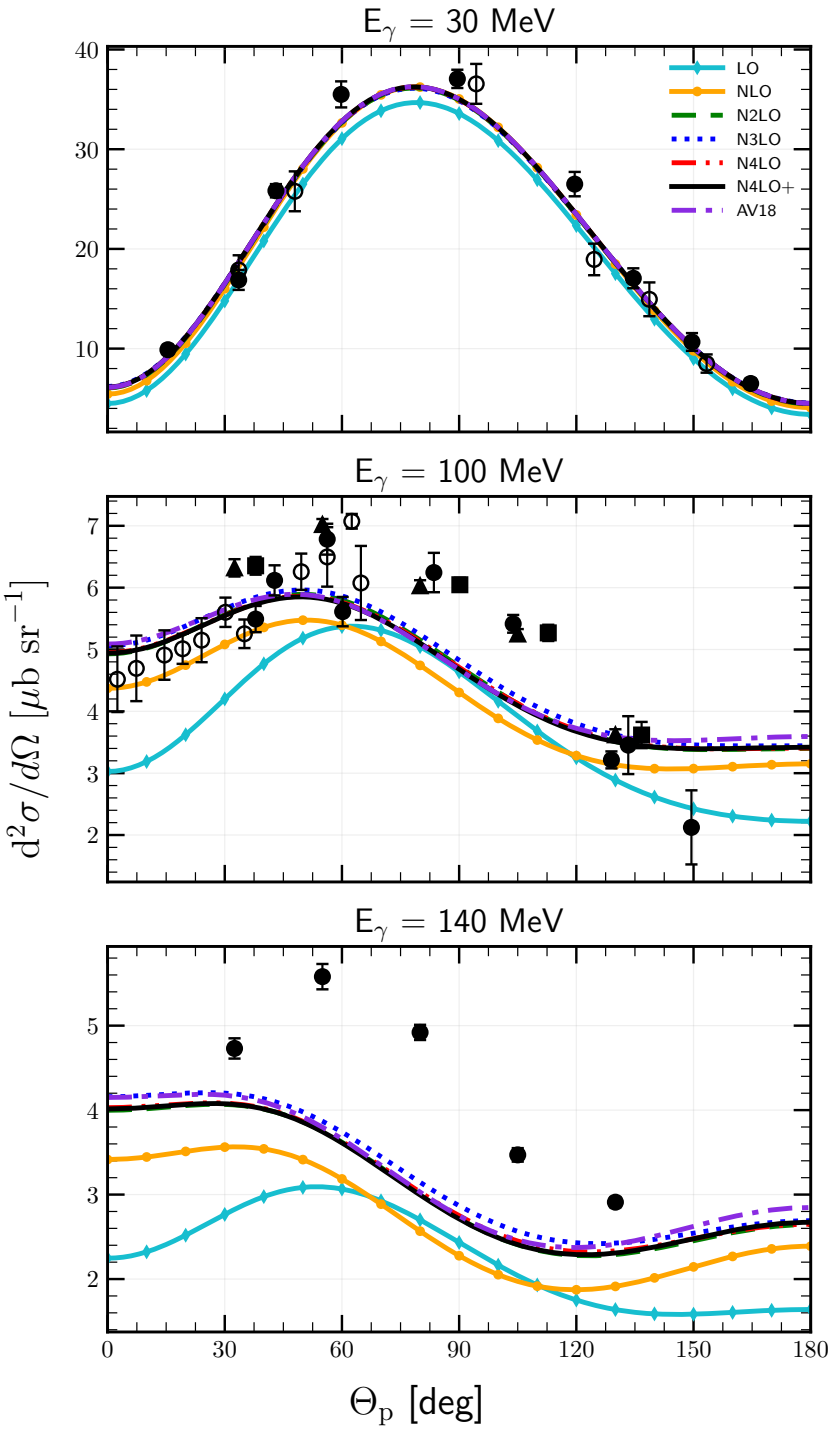

Figure 4.3: Differential cross section as a function of the outgoing proton angle in the center of mass frame for the photon's energy 30 MeV (top), 100 MeV (middle) and 140 MeV (bottom). Results are obtained using potential with different chiral orders (from LO to N^{4}LO+) with cutoff parameter $\Lambda = 450$ MeV. For the sake of comparison, predictions obtained with AV18 potential are on both figures as well. Data points (filled and empty circles) are from [?] for (30 and 100 meV) and [?] (for energy 140 MeV).

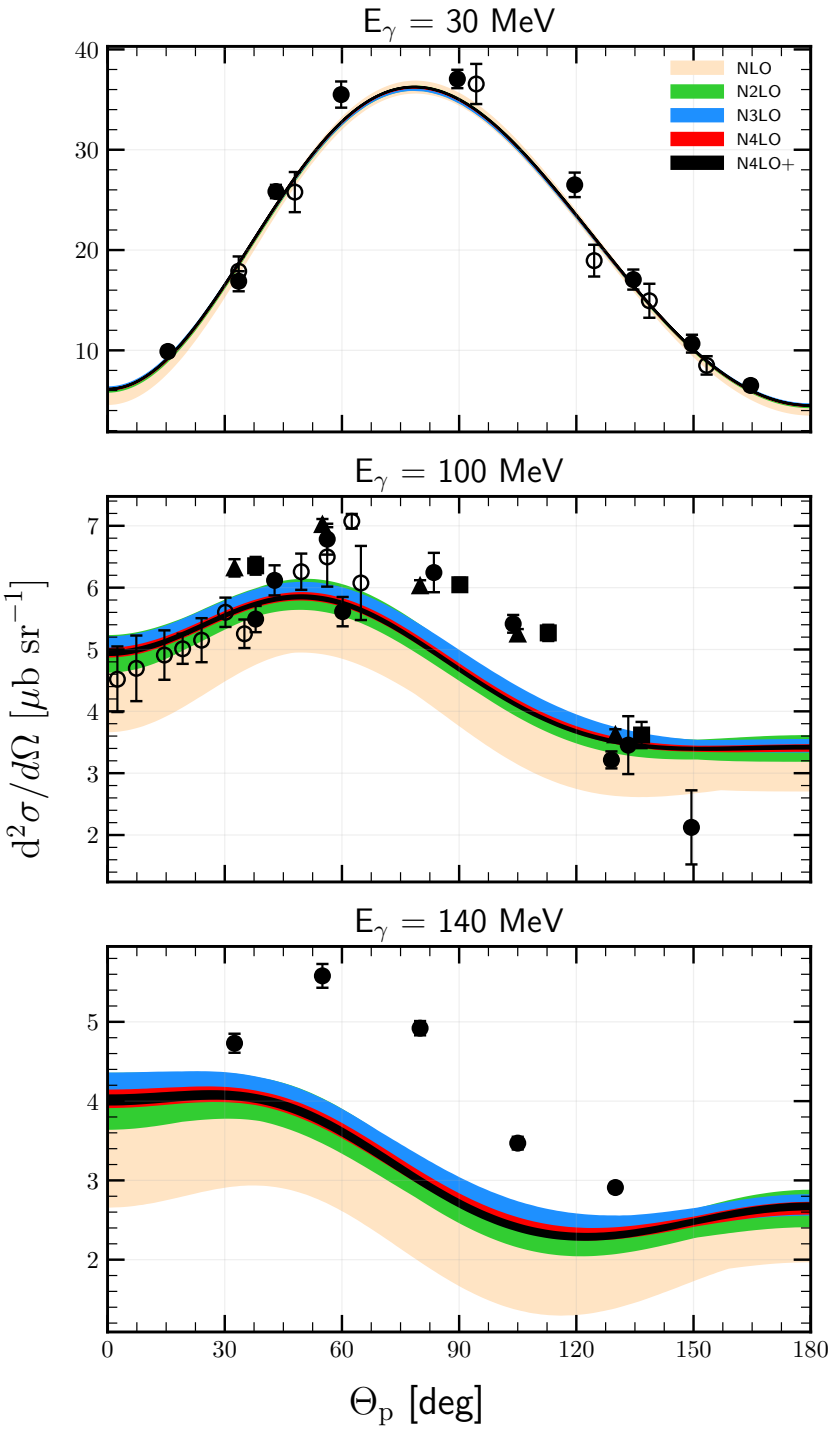

Figure 4.4: Truncation error's bands for the differential cross section as a function of the outgoing proton angle in the center of mass frame The photon's energy is 30 MeV (top pane), 100 MeV (middle) and 140 MeV (bottom). Results are obtained using potential with different chiral orders (from LO to N^{4}LO+) with cutoff parameter $\Lambda = 450$ MeV. Data points (filled and empty circles) are from [?] for (30 and 100 meV) and [?] (for energy 140 MeV).

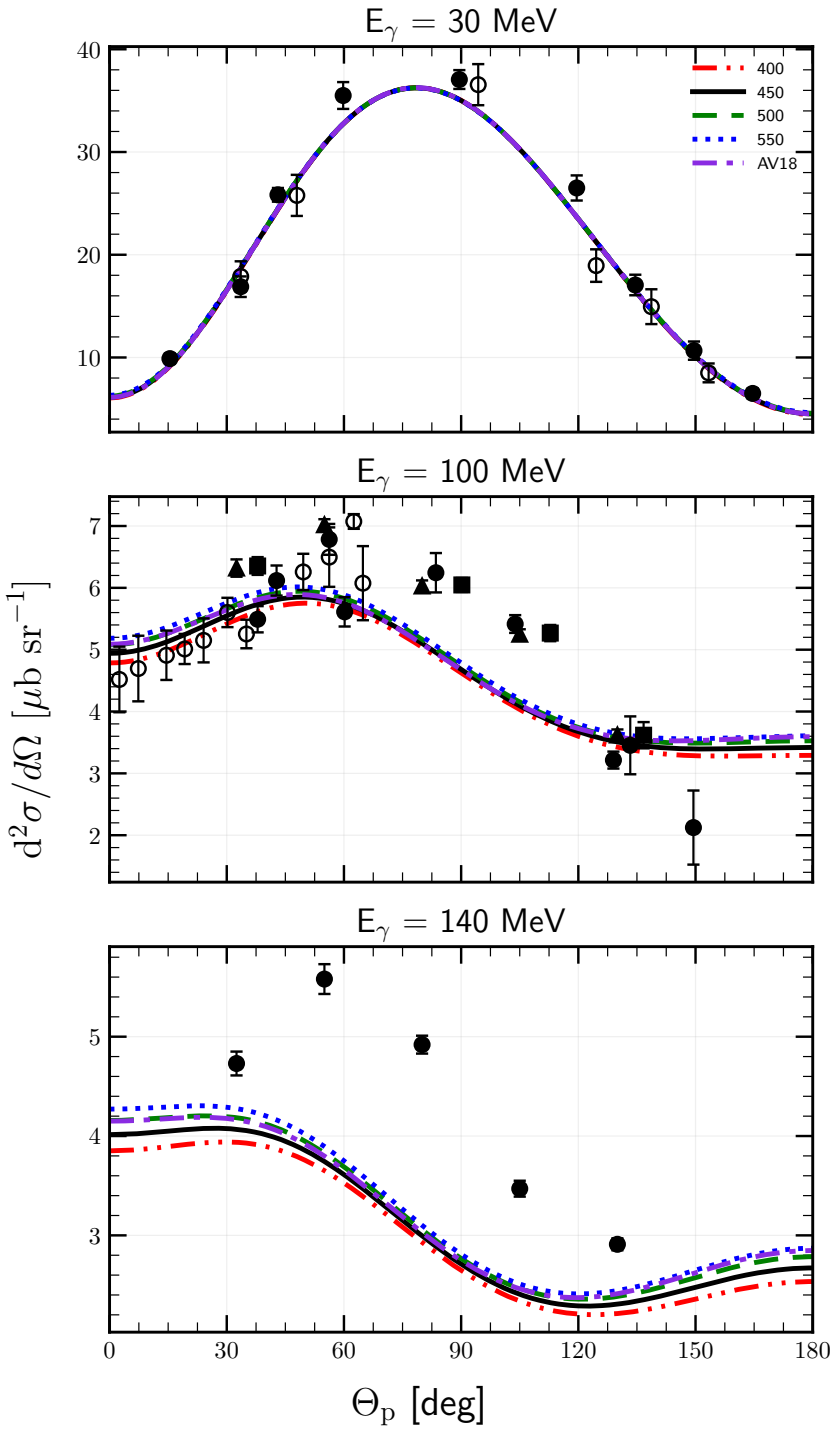

Figure 4.5: Truncation error's bands for the differential cross section as a function of the outgoing proton angle in the center of mass frame ThDifferential cross section as a function of the outgoing proton angle in the center of mass frame for the photon's energy is 30 MeV (top pane), 100 MeV (middle) and 140 MeV (bottom). The double-dotted-dashed red line presents results obtaining with a cutoff values $\Lambda = 400$ MeV, solid black line - 450 MeV, dashed green line - 500 MeV and dotted blues line - 550 MeV. For the sake of comparison, predictions obtained with AV18 potential (purple dotted-dashed line). Data points (filled and empty circles) are from [?] for (30 and 100 meV) and [?] (for energy 140 MeV).

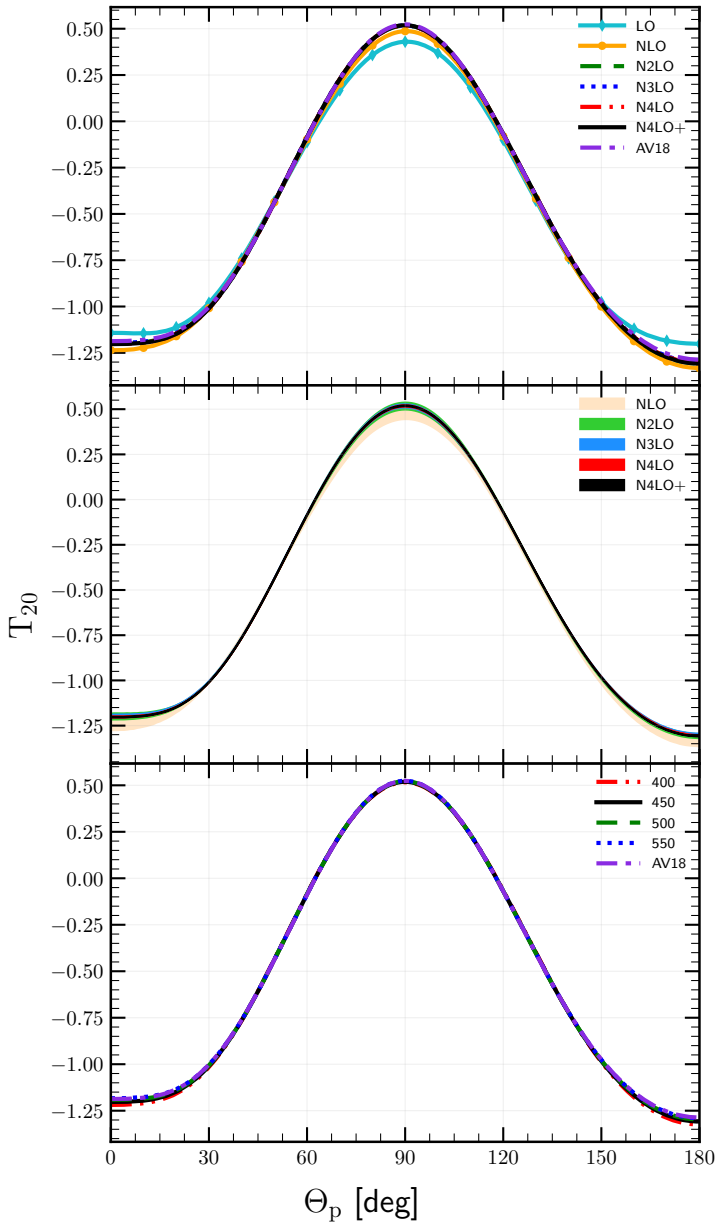

Figure 4.6: Tensor analyzing power T_{20} as a function of the outgoing proton angle in the center of mass frame for the photon's energy 100 MeV. Top figure presents results obtained using potential with different chiral orders (from LO to N^{4}LO+) with cutoff parameter $\Lambda = 450$ MeV. The middle pane shows truncation errors for each chiral order starting from NLO and bottom figure presents a cutoff dependency (chiral potential N^{4}LO+). For the sake of comparison, predictions obtained with AV18 potential are on figures as well.

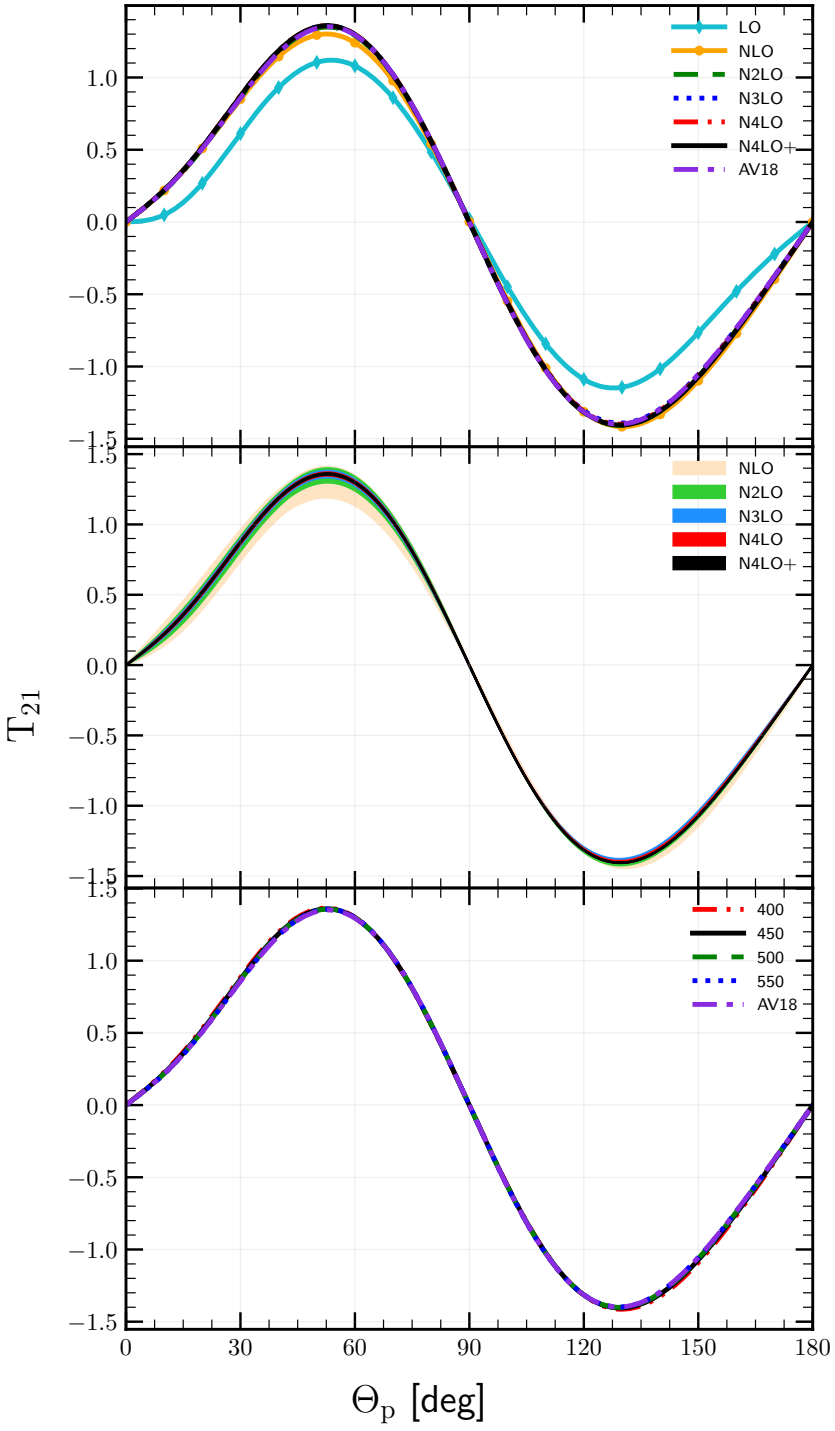

Figure 4.7: The same as on 4.6 but for the tensor analyzing power component T_{21}

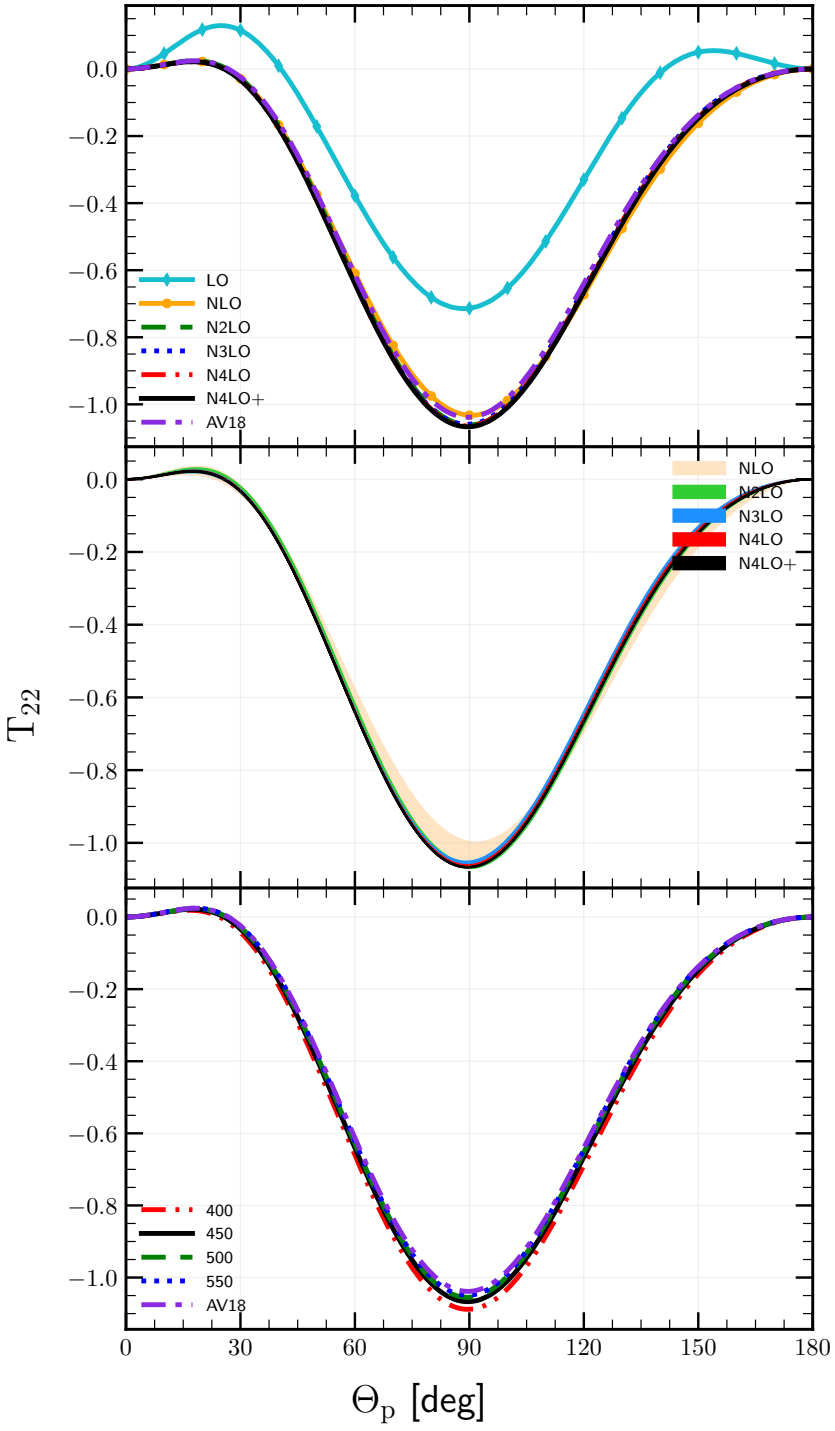

Figure 4.8: The same as on 4.6 but for the tensor analyzing power component T_{22}

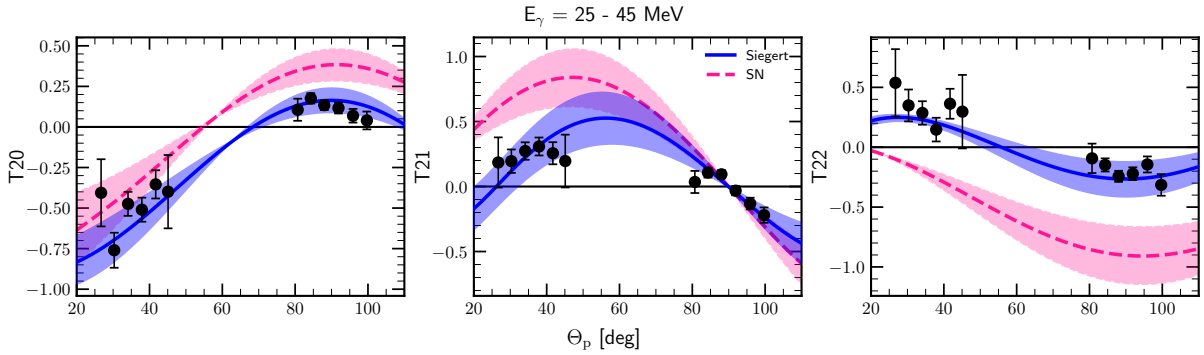

Figure 4.9: Tensor analyzing powers T_{20}, T_{21} and T_{22} as a functions of the outgoing proton angle θ_p (in the center of mass frame). Solid blue line is a mean value of my predictions obtained with a SMS potential at N^{4}LO+ chiral order and with $\Lambda = 450$ MeV at energy values from 25 to 45 MeV and where SN current was used together with Siegert approach. Pink dashed line is similar prediction but with SN only. The corresponding bands show the deviation of predictions in the regarded energy region. Filled circles are experimental data from [**?**] for the analogous energy span.

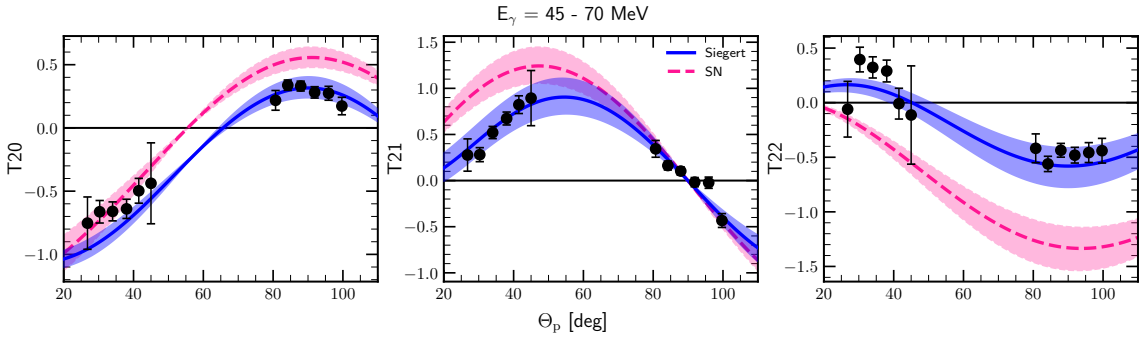

Figure 4.10: The same as on the Fig. 4.9 but for energy bin 45 - 70 MeV

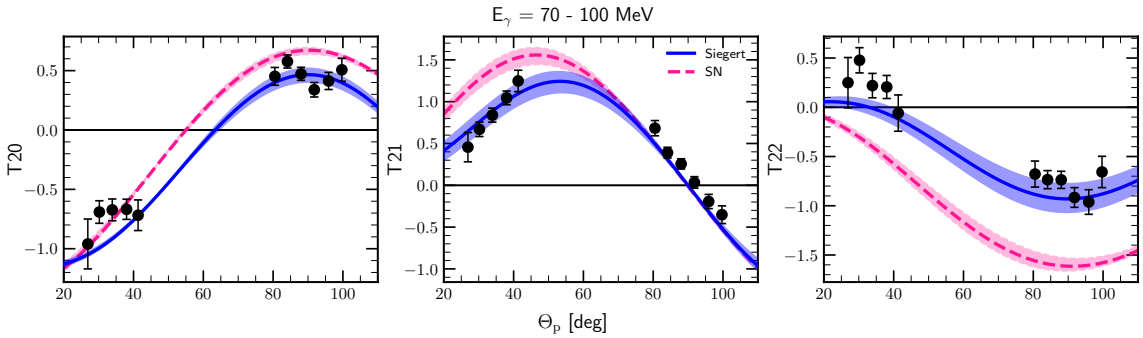

Figure 4.11: The same as on the Fig. 4.9 but for energy bin 70 - 100 MeV

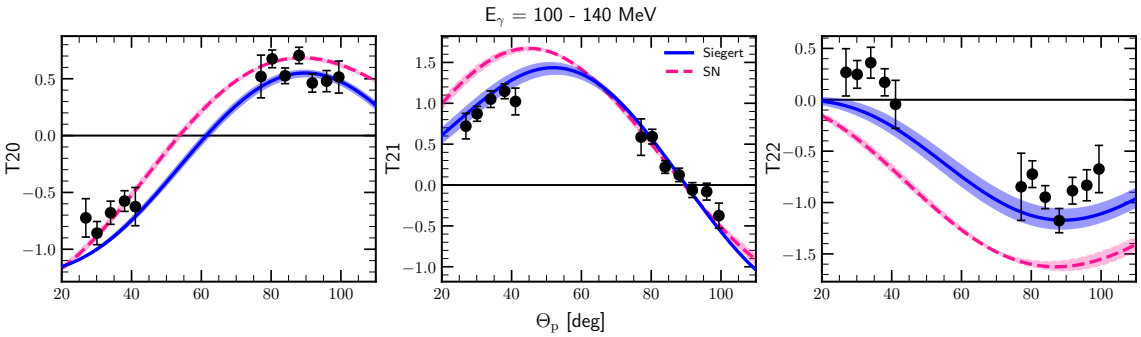

Figure 4.12: The same as on the Fig. 4.9 but for energy bin 100 - 140 MeV

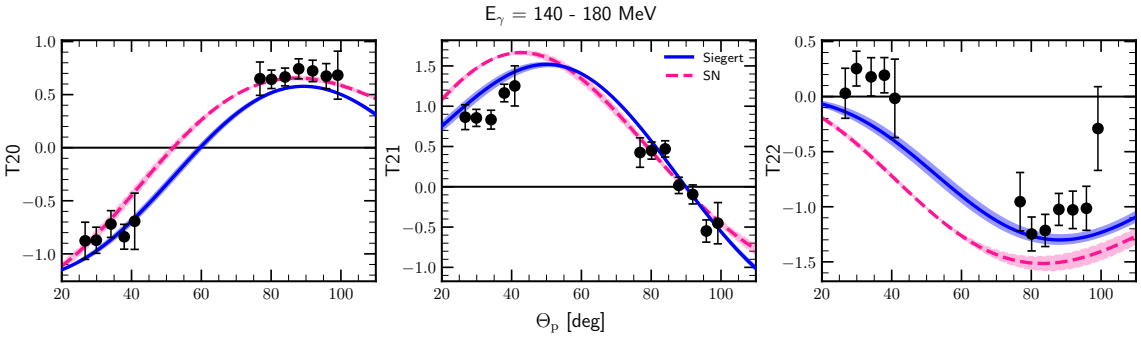

Figure 4.13: The same as on the Fig. 4.9 but for energy bin 140 - 180 MeV

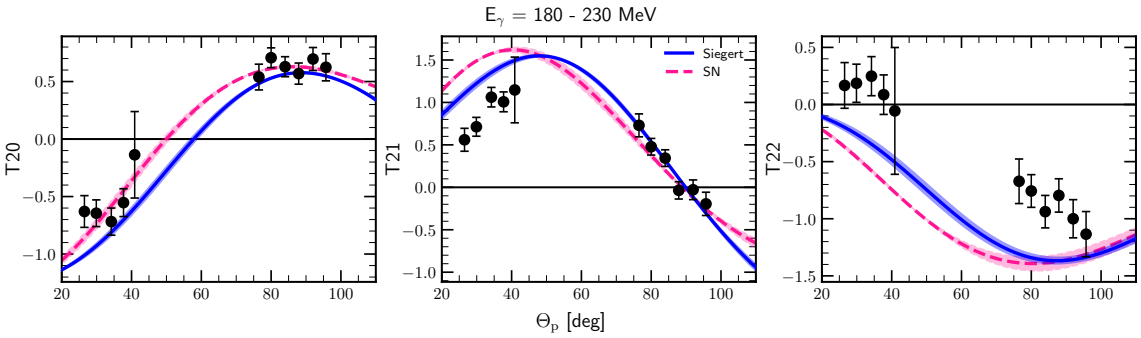

Figure 4.14: The same as on the Fig. 4.9 but for energy bin 180 - 230 MeV

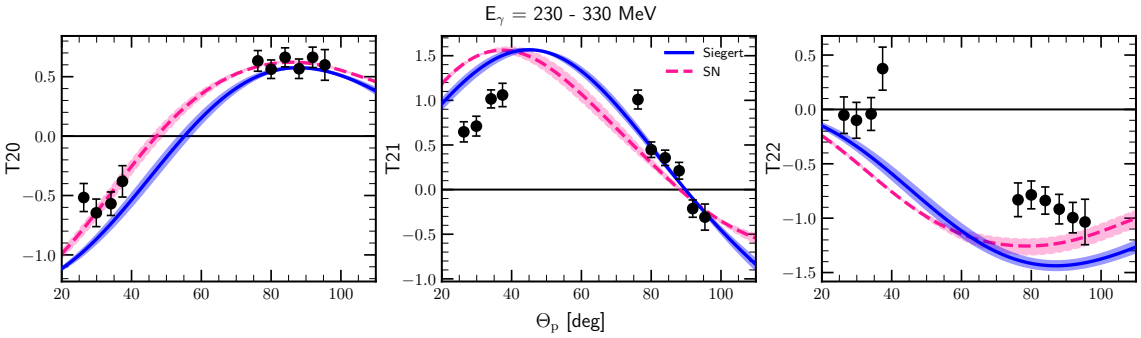

Figure 4.15: The same as on the Fig. 4.9 but for energy bin 230 - 330 MeV

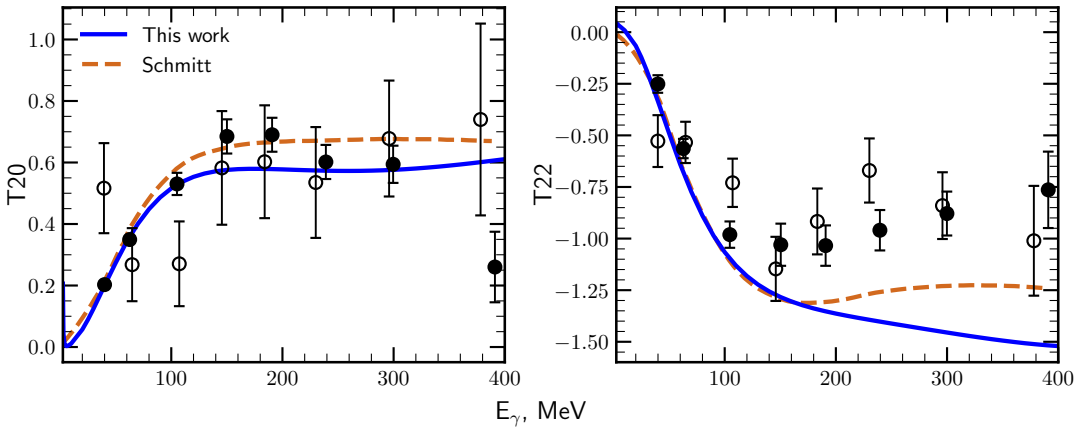

Figure 4.16: Tensor analyzing powers T_{20} and T_{22} as a functions of the photon energy E_γ with fixed outgoing proton angle $\theta_p = 88°$ (in the center of mass frame). My predictions (blue solid line) are obtained with SMS potential at chiral order N^{4}LO+ and with cutoff parameter $\Lambda = 450$ MeV. Dashed brown line presents calculations from [?]. Experimental data is taken from [?] (filled circles) and [?] (empty circles).

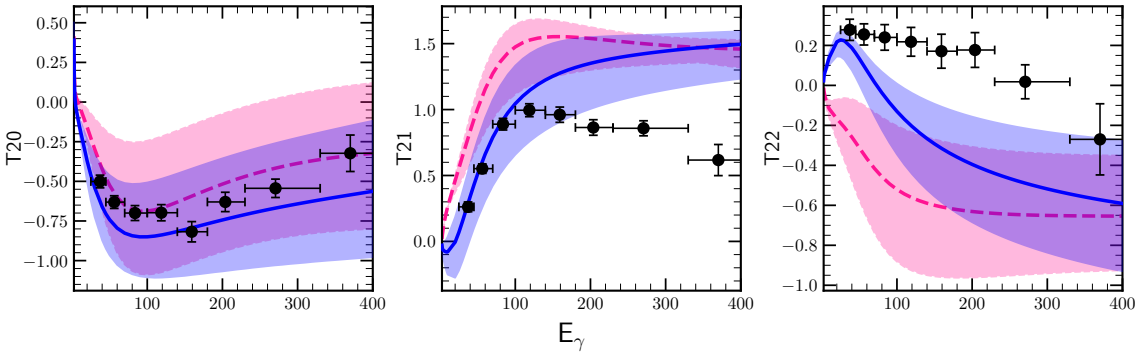

Figure 4.17: Tensor analyzing powers T_{20}, T_{21} and T_{22} as a functions of the photon's energy within the outgoing proton's angle range $24° - 48°$ (in the center of mass frame). Solid blue line is a mean value of my predictions obtained with SMS potential at N^{4}LO+ chiral order and with $\Lambda = 450$ MeV at energy values from 25 to 45 MeV within a given angles range and where SN current was used together with Siegert approach. Pink dashed line is similar prediction but with SN only. The corresponding bands show the deviation of predictions in the regarded energy region. Filled circles are experimental data from [?] for the analogous energy span.

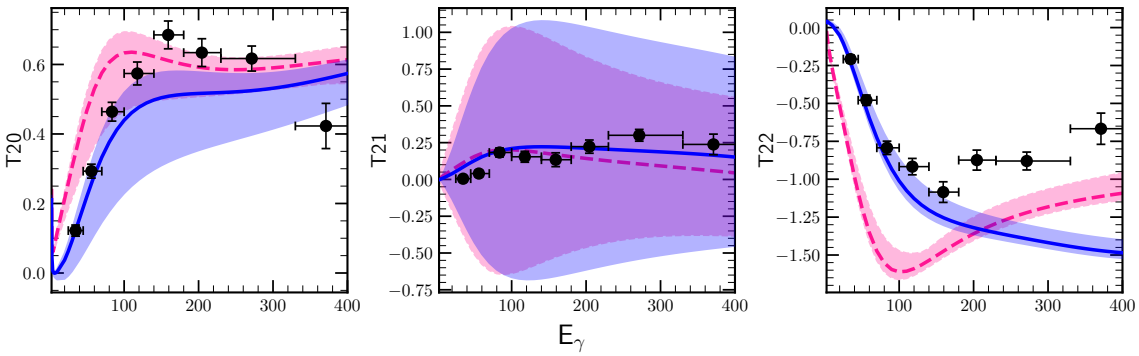

Figure 4.18: The same as on the Fig. 4.17 but for the angles' range $70° - 102°$.

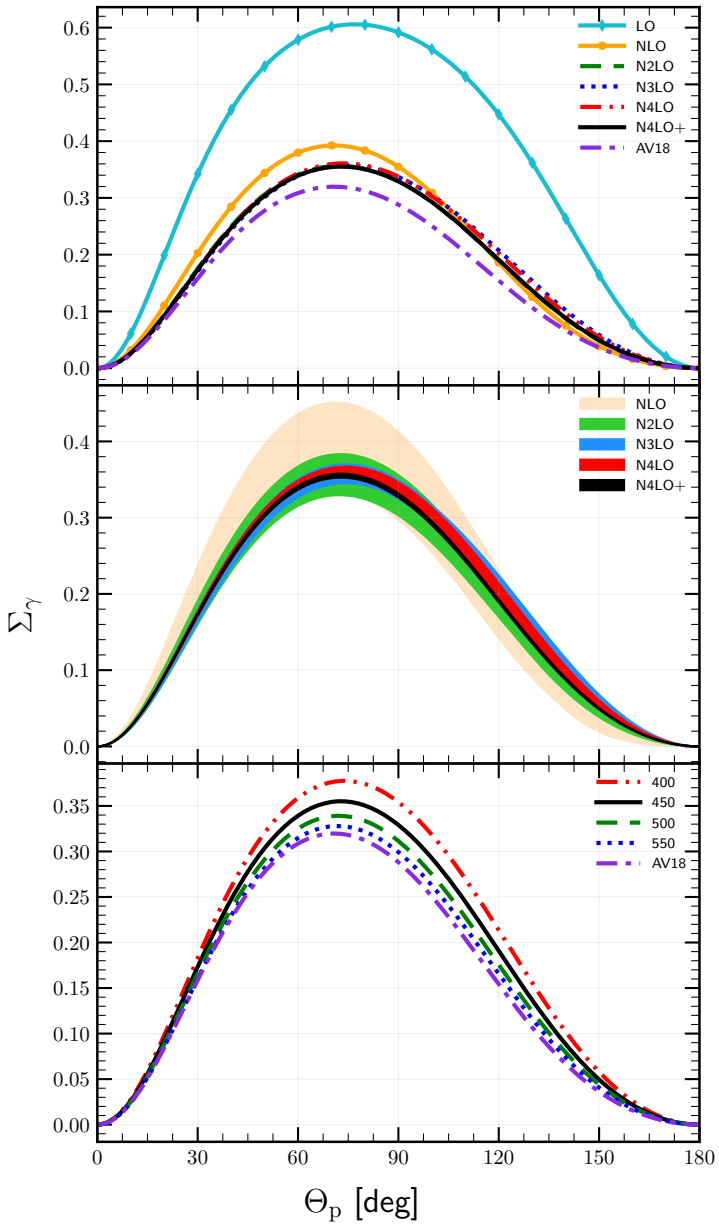

Figure 4.19: The photon asymmetry Σ_γ as a function of the outgoing proton angle in the center of mass frame for the photon's energy 100 MeV. Top figure presents results obtained using potential with different chiral orders (from LO to N^{4}LO+) with cutoff parameter $\Lambda = 450$ MeV. The middle pane shows truncation errors for each chiral order starting from NLO and bottom figure presents a cutoff dependency (chiral potential N^{4}LO+). For the sake of comparison, predictions obtained with AV18 potential are on figures as well.

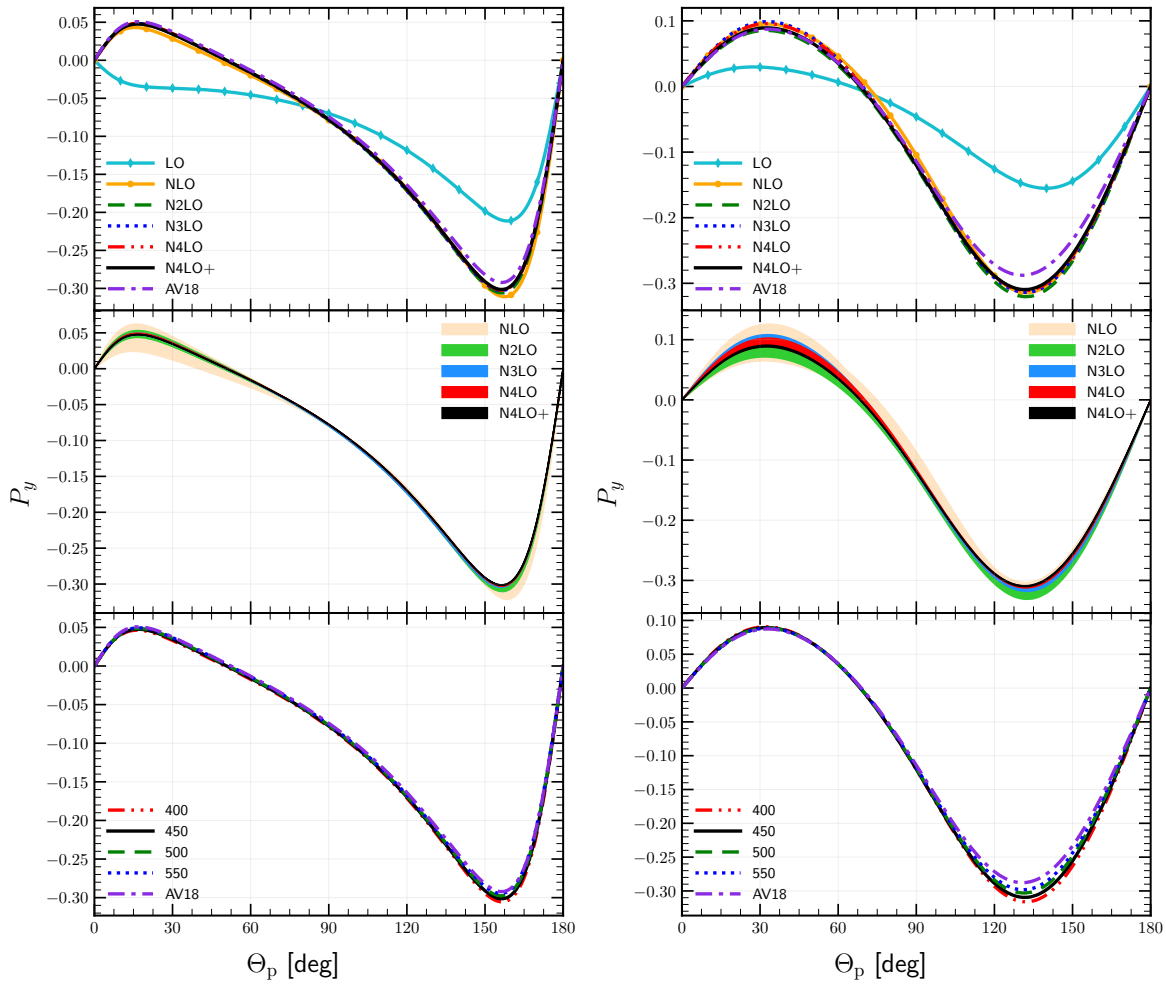

(a) $E_\gamma = 30$ MeV (b) $E_\gamma = 100$ MeV

Figure 4.20: Proton polarisation P_y as a function of the outgoing proton angle in the center of mass frame for the photon's energy 30 MeV (a) and 100 MeV (b). Top figure presents results obtained using potential with different chiral orders (from LO to N^{4}LO+) with cutoff parameter $\Lambda = 450$ MeV. The middle pane shows truncation errors for each chiral order starting from NLO and bottom figure presents a cutoff dependency (chiral potential N^{4}LO+). For the sake of comparison, predictions obtained with AV18 potential are on figures as well.

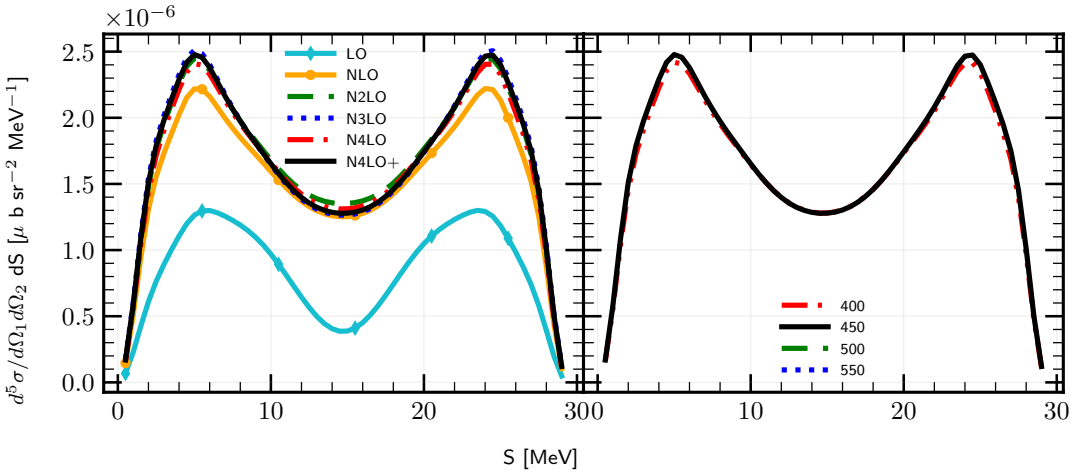

Figure 4.21: The five-fold differential cross section for the photon energy $E_\gamma = 40$ MeV. The left figure presents results obtained using potential with different chiral orders (from LO to N^{4}LO+) with cutoff parameter $\Lambda = 450$ MeV. The right figure presents a cutoff dependency (chiral potential N^{4}LO+).

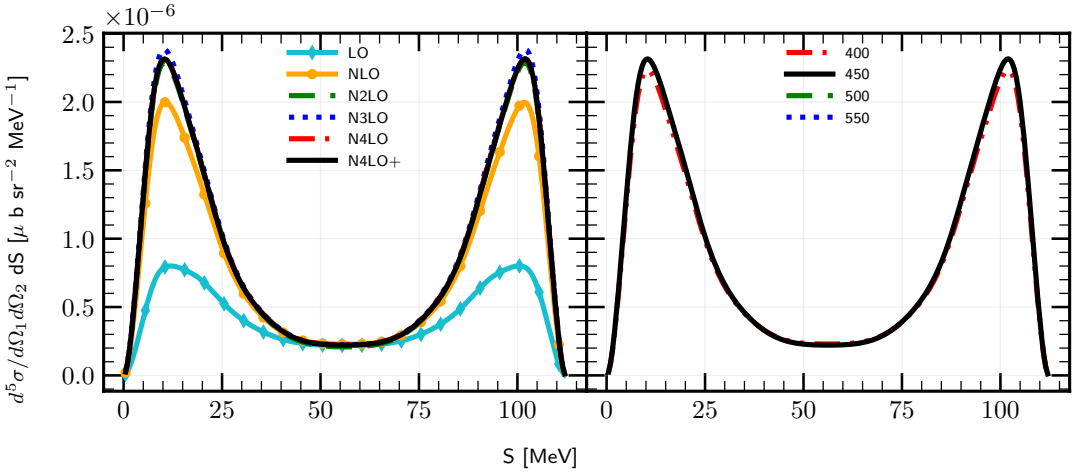

Figure 4.22: The same as on Fig. 4.21 but for the photon energy $E_\gamma = 120$ MeV

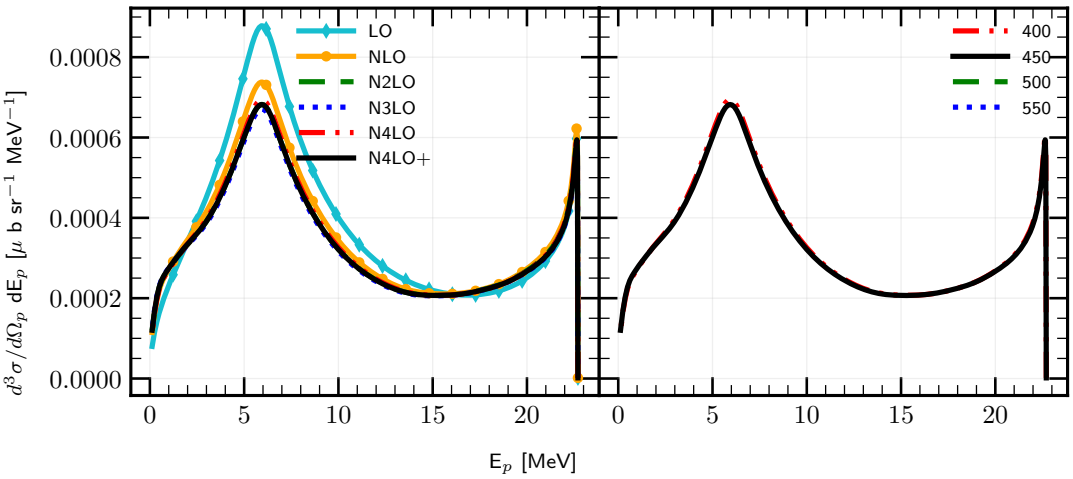

Figure 4.23: Inclusive cross section... E$_\gamma$ = 40 MeV, $\theta = 60°$

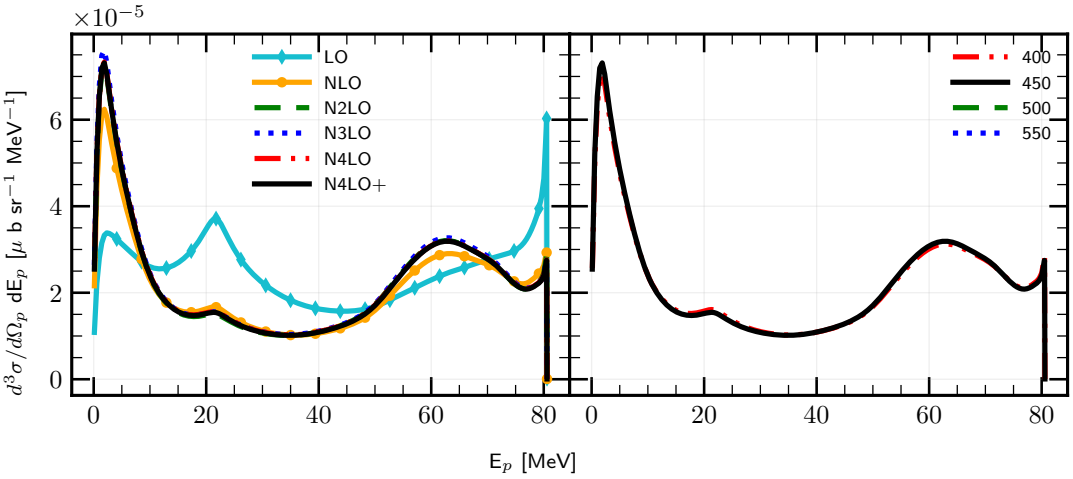

Figure 4.24: Inclusive cross section... E$_\gamma$ = 120 MeV, $\theta = 60°$

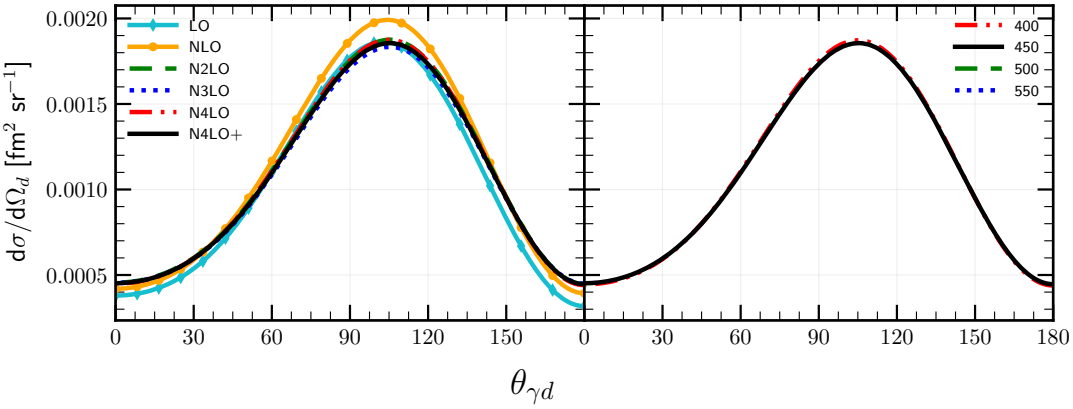

Figure 4.25: Differential cross section for the d-γ two-body photodisintegraion of ^{3}He as a function of the dγ angle. The initial photon energy $E_\gamma = 40$ MeV.

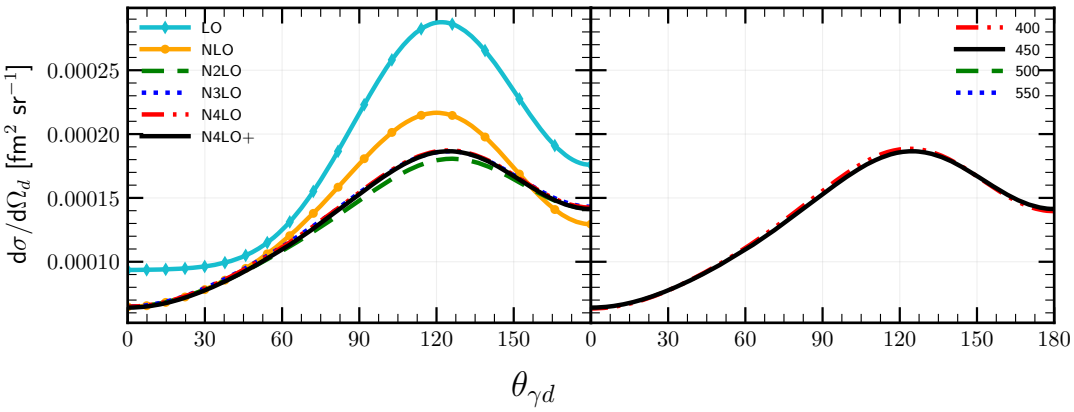

Figure 4.26: The same as on Fig. 4.25 but for the photon energy $E_\gamma = 120$ MeV